DOE/BC/15202-2

(OSTI ID: 807241)

NMR Characterizations of Properties of Heterogeneous Media

A

Semi-Annual Progress Report

for the period

May 2002 - October 2002

A. Ted Watson, Jack Phan, Jinsoo Uh, Rudi Michalak and Song Xue

Department of Chemical Engineering, Texas A&M University

College Station, Texas 77843-3122

November 29, 2002

DOE Award Number DE-AC26-99BC15202

Texas Engineering Experiment Station (TEES)

Texas A&M University

College Station, Texas 77843-3122

Disclaimer

Abstract

The overall goal of this project is to develop reliable nuclear magnetic resonance (NMR) methods for resolving macroscopic properties important for describing the flow of fluids through heterogeneous permeable media. While the understanding and description of flow in heterogeneous permeable media has been limited, nuclear magnetic resonance imaging (MRI) provides unprecedented opportunities for resolving fluid states and the associated media properties at a fine scale. In Stage I, we develop advanced core analysis methods for fully characterizing properties of heterogeneous media. In Stage II, we perform experiments on selected core samples, using the results from Stage I, to obtain data which can be used to develop methods to predict macroscopic properties from well-log observable quantities. In Stage III, we develop and evaluate methods for predicting absolute permeability, and evaluate a novel method for predicting relative permeability. The progress during the seventh reporting period is summarized in the following and detailed reports are provided in this document.

During this reporting period, the facilities to house our new NMR imager have been completed, and the equipment is being delivered and installed. We have completed modifications to an existing computer code to incorporate all three spatial directions when simulating two-phase displacement experiments. New experimental designs that will provide for more reliable estimation of permeability distributions were evaluated. We designed and built a new core holder to incorporate one of the new experimental designs.

Contents

List of Figures

List of Tables

1 Introduction

The detailed knowledge of heterogeneous media properties associated with fluid flow within porous media is essential to the success of petroleum reservoir management and characterization. However, the study of heterogeneous porous media has been limited by the lack of methods to spatially resolve properties within core samples. Conventional methods utilize inflow and outflow measurements, and often do not adequately resolve heterogeneities. Nuclear magnetic resonance imaging (MRI) gives non-invasive measurements within media. Suitable interpretation of the data provides unprecedented opportunities for resolving fluid states to determine macroscopic properties important for describing the flow behavior of multiple phases in reservoirs.

In this project, we develop advanced core analysis tools utilizing magnetic resonance imaging techniques to determine macroscopic properties of porous media. We have conducted a series of experiments on a suite of samples from a domestic reservoir and have developed advanced methodologies to determine the basic properties. The collected NMR experimental data are used to determine distributions of porosity and absolute permeability. That information is used together with data collected from displacement experiments to determine multi-phase flow properties such as relative permeability and capillary pressure functions. We are also investigating improved methods for prediction absolute permeabilities from well-log observable properties.

During the current reporting period, there was notable progress related to our NMR experimental capabilities. Our new NMR imager has now been delivered and is being installed in a laboratory at Colorado State University that was refurbished to house that equipment. Section 2 describes the progress associated with the new laboratory in detail. A new research scientist, with extensive experience in NMR, was hired to manage the operation and maintenance of the new equipment. With the completion of the MRI installation, which is expected by December 15, 2002, we will be prepared to finish the experimental portion of this project.

In section 3, the numerical work for estimating two-phase flow functions while accounting for spatial variations in porosity and permeability is described. In section 4, we evaluate issues associated with the identifiability of permeability distributions from velocity images. We determine that new experimental designs will provide more reliable estimates of the permeability distributions. In section 5, we present plans for new core holders to implement one of those experimental designs.

There have also been several academic achievements during the reporting period. Two manuscripts related to the determination of porosity and permeability distributions in porous media

were published (Watson *et al.* 2001; Watson *et al.* 2002). Another part of the project related to determining surface relaxivity using an NMR method was presented at the *Annual Meeting of the American Institute of Chemical Engineers,* held in Indianapolis, Indiana, in November.

2 Progress of NMR Laboratory Setup

Some experimental elements of this project have been delayed pending the installation of a new MRI system at Colorado State University. Further delays were encountered in preparing a suitable laboratory site to stage the MRI equipment. The equipment has now been delivered, and is being set up. The equipment set up and training should be completed by December 15, 2002. While the equipment purchase and laboratory set up is not funded by this project, the delays may be better appreciated with some idea of the magnitude of this effort. Consequently, we present some aspects of the laboratory development in this section.

The building of an MRI laboratory requires three steps: the preparation of the site, the delivery of the equipment, and the buildup of the spectrometer. Steps one and two have been completed for our MRI, while step three is in progress.

Before the arrival of the unit, the laboratory room was prepared with regard to electrical and water pipe installations. The accessibility (way of transportation through doors and around corners) and the weight carrying performance of the underground have been checked.

The MRI magnet weighs approximately 6,000 pounds. It has been placed on a solid cement base which is raised by about 4 inches relative to the main floor. The final placement of the magnet is a delicate task with respect to maneuvering space (see Figs. 1 and 2). The magnet is housed in an RF-cage (see Fig. 3). The copper-foil 'wrapped' room acts as a Faraday cage, shielding the electromagnetic radiation that is created during the experiment. This addresses the capacity of this radiation to disturb neighboring facilities by sending electromagnetic noise features into their systems and, even more important, the coupling back into parts of the MRI system, which would reduce the signal-to-noise factor of the experiment. The cage effectively limits this problem.

To a certain degree, the cage also helps in meeting the safety regulations for operating strong magnetic fields. These concern the stray field which occurs in the vicinity of the magnet unit and which extends into the surrounding space. The acceptable limit for public access is given by the so called '5 Gauss line'. Thanks to the help of the cage, the critical line is well within the laboratory limits so that the only further safety requirement is to restrict the access to the laboratory to

Figure 1: A local contractor's fork lift maneuvers the magnet into the building

Figure 2: The final positioning of the magnet in the RF-cage is an inch-by-inch job

Figure 3: The copper-foil covered RF-cage shields electromagnetic radiation to and from the system

authorized personnel.

Step three consists of the setup of the transmitter array, the workstation (including a number of secondary processing units and the connection to the local computer network), the receiver unit, a number of control devices (cryogen meter, temperature controller, etc.), and the installation of the shim and gradient coils (Fig. 4). Finally, the MRI magnet and the superconducting and room temperature shim coils have to be set to the permanent operation fields.

At this point, all physical installations have been completed. What remains to be done is the final test for full functionality and the setting of the fine tuning room temperature magnetic shim fields. The functionality test and the test of the purchased probes can only be performed when the magnet is set to field, because otherwise no NMR/MRI signal will be obtained. The setting of the magnetic fields is a crucial and delicate part of the installation. The precision by which the strength of the main field, its decay with time, and its spacial homogeneity pattern can meet the default values influences the signal-to-noise ratio which can be achieved for the MRI experiments.

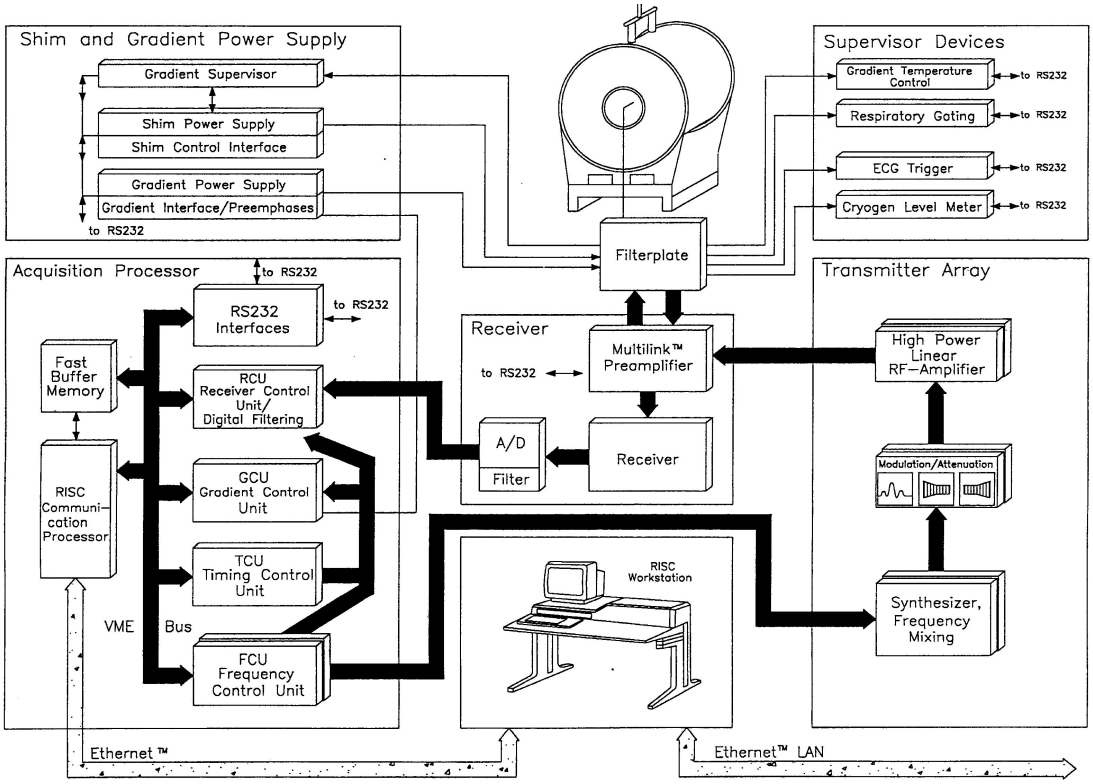

Figure 4: A block diagram of the MRI spectrometer setup

3 Determination of Multiphase Flow Properties

3.1 Introduction

Multiphase flow functions (relative permeability and capillary pressure curves) are required to simulate the flow of multiple fluid phases through porous media. These are normally determined from experimental data measured during displacement experiments on laboratory core samples. Conventionally, these estimates are based on the assumption that the porosity and permeability are uniform within the sample. Spatial variations in those properties, which are known to exist, will lead to associated errors in the estimates of the multiphase flow functions.

For the first time, the entire distributions of the porosity and permeability within samples will be known using the methods developed in our project. We will account for the spatial variations in those properties when determining the multiphase flow functions with displacement experiments.

The process for determining multiphase properties from the displacement experimental data is implemented with the computer program SENDRA. This program is built around a two- dimensional, two-phase, black-oil simulator (Petec Software & Services, 2000). We will extend the

simulator to represent all three spatial coordinate directions so that the entire porosity and permeability distributions are accounted for in the estimation of multiphase flow properties. In this section, we summarize the work performed in extending the simulator to represent all three spatial dimensions.

3.2 Theory

Mathematical model

The mathematical description used to simulate the flow of fluid in porous materials is based on local volume-averaging concepts (Slattery 1981). A Darcy equation and equation of continuity are written for each fluid phase:

$$\overrightarrow{v_f} = -\frac{Kk_{rf}}{\mu_f} \cdot (\bigtriangledown p_f - \rho_f \overrightarrow{g}) \tag{1}$$

$$\frac{\partial \phi \rho_f S_f}{\partial t} = -\nabla \cdot (\rho_f \overrightarrow{v_f}) + q_f \qquad f = n, nw \tag{2}$$

where w and nw refer to wetting and non-wetting fluid phases, respectively. Combining the Darcy equation and mass conservation equation by eliminating the velocity $\overrightarrow{v_f}$, we obtain the following set of differential equations describing two-phase flow:

$$\nabla \cdot [\frac{\rho_f K k_{rf}}{\mu_f} (\nabla p_f - \rho_f g \nabla h)] + q_f = \frac{\partial (\phi \rho_f S_f)}{\partial t} \qquad f = n, nw \tag{3}$$

The capillary pressure relation and the summation of the phase saturations provide two additional equations:

$$p_c = p_{nw} - p_w \tag{4}$$

$$S_{nw} + S_w = 1 \tag{5}$$

Boundary conditions

In order to solve the differential equations describing flow, it is necessary to specify appropriate boundary conditions. Several production and injection cases could be realized in an experimental study (Petec Software & Services, 2000), such as the cases listed below:

- Production at constant pressure
- Production with constant total rate

- Injection of a single fluid phase at constant pressure
- Injection of both fluid phases at constant pressure
- Injection of a single fluid phase with constant rate
- Injection of both fluid phases with constant rate

Specification of pressures at sources and sinks normally presents no special problem in numerical representation. Fluid phase rates of injection and production present a more complicated situation than pressure does since some procedures are required to allocate the rate among the several grid blocks communicating with the given source/sink. In our core flood simulation, a non-flow condition is imposed at a rectangular domain boundary as shown in Fig. 5. Fluid injection and production take place within grid blocks in which sources or sinks are specified. We inject one fluid phase (oil) into the sample which is completely saturated with a second fluid phase (water). A constant pressure is maintained at the outlet end. A method developed by Nolen and Berry has been used

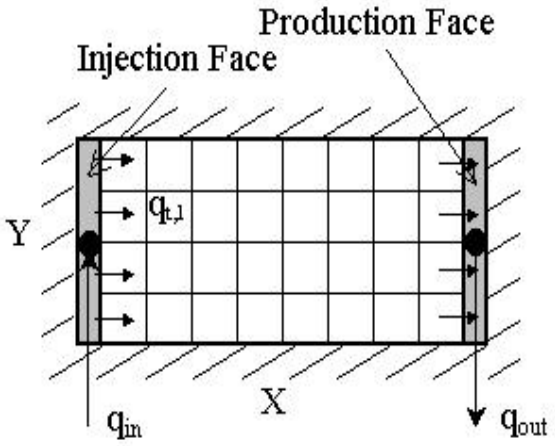

Figure 5: Representation of a rectangular shaped sample

to perform the explicit allocation of injected flow according to the total transmissibility (Nolen and Berry 1972). This method assumes that the difference of pressure between the injection face and an adjacent grid block is the same for all blocks communicating with the source. Under this assumption, it can be shown that the total flow for any injection block is approximated by

$$q_{t,l} = \frac{T_{w,l} + T_{o,l}}{\sum_{l=1}^{L} T_{w,l} + T_{o,l}} q_t, \tag{6}$$

where L is the total number of blocks communicating with a given source and the transmissibilities T_o and T_w are defined as $T_o = \frac{b_o K k_{ro}}{\mu_o}$ and $T_w = \frac{b_w K k_{rw}}{\mu_w}$, respectively.

Matrix structure and matrix solvers

An unconditionally stable fully implicit finite-difference method is used to calculate grid block pressures and saturations. The grid system is block-centered. The original version of SENDRA represents only two spatial directions. We have modified the computer code so that all three spatial directions are represented. The domain has $(N_x \times N_y \times N_z)$ grid blocks, instead of $(N_x \times N_y \times 1)$ grid blocks for the original version of SENDRA, where each block is represented by (i, j, k), $i = 1, 2, ..., N_x, j = 1, 2, ...N_y$, and $k = 1, 2, ..., N_z$. The equations for the wetting and non-wetting fluid phases are solved simultaneously.

Using the finite difference scheme with the block centered grid system, the discretized form for Eq. 3 can be written in the following forms. Here, the z-component of the derivative is added for the 3D case:

$$\Delta_x T_{nw,x}(\Delta_x \Phi_{nw,x}) + \Delta_y T_{nw,y}(\Delta_y \Phi_{nw,y}) + \Delta_z T_{nw,z}(\Delta_z \Phi_{nw,z}) = \Delta_t(\phi b_{nw} S_{nw}) + q_{nw} \tag{7}$$

$$\Delta_x T_{wx}(\Delta_x \Phi_{wx}) + \Delta_y T_{wy}(\Delta_y \Phi_{wy}) + \Delta_z T_{wz}(\Delta_z \Phi_{wz}) = \Delta_t(\phi b_w S_w) + q_w \tag{8}$$

where $\Phi_{nw} = p_{nw} + \rho_{nw} g h$, $\Phi_w = p_w + \rho_w g h$ and Δ_x, Δ_y and Δ_z are spatial difference operators and Δ_t is a time difference operator. After replacing the derivatives by difference quotients, we have:

$$\begin{aligned}
\frac{\partial}{\partial x}\left(T_f \frac{\partial \Phi}{\partial x}\right)\Big|_{i,j,k} &= \frac{T_{f,i+\frac{1}{2},j,k}\left(\Phi_{i+1,j,k} - \Phi_{i,j,k}\right) - T_{f,i-\frac{1}{2},j,k}\left(\Phi_{i,j,k} - \Phi_{i-1,j,k}\right)}{(\Delta x)^2} \\
&= \frac{1}{(\Delta x)^2}\left\{\Phi_{i-1,j,k}\left(T_{f,i-\frac{1}{2},j,k}\right) + \Phi_{i,j,k}\left(-T_{f,i-\frac{1}{2},j,k} - T_{f,i+\frac{1}{2},j,k}\right) + \Phi_{i+1,j,k}\left(T_{f,i+\frac{1}{2},j,k}\right)\right\}
\end{aligned}$$

$$\frac{\partial}{\partial y}\left(T_f \frac{\partial \Phi}{\partial y}\right)\Big|_{i,j,k} = \frac{1}{(\Delta y)^2}\left\{\Phi_{i,j-1,k}\left(T_{f,i,j-\frac{1}{2},k}\right) + \Phi_{i,j,k}\left(-T_{f,i,j-\frac{1}{2},k} - T_{f,i,j+\frac{1}{2},k}\right) + \Phi_{i,j+1,k}\left(T_{f,i,j+\frac{1}{2},k}\right)\right\}$$

$$\frac{\partial}{\partial z}\left(T_f \frac{\partial \Phi}{\partial z}\right)\Big|_{i,j,k} = \frac{1}{(\Delta z)^2}\left\{\Phi_{i,j,k-1}\left(T_{f,i,j,k-\frac{1}{2}}\right) + \Phi_{i,j,k}\left(-T_{f,i,j,k-\frac{1}{2}} - T_{f,i,j,k+\frac{1}{2}}\right) + \Phi_{i,j,k+1}\left(T_{f,i,j,k+\frac{1}{2}}\right)\right\}$$

We define the functions:

$$\begin{aligned}
f(\mathbf{X}_{i,j,k}) &= \left\{\ \Delta_x\left(T_f \Delta_x \Phi\right) + \Delta_y\left(T_f \Delta_y \Phi\right) + \Delta_z\left(T_f \Delta_z \Phi\right)\ \right\}_{i,j,k} \\
h(\mathbf{X}_{i,j,k}) &= \frac{1}{\Delta t}\left(\phi b S\right)_{i,j,k}
\end{aligned}$$

where $\mathbf{X}_{i,j,k} \equiv (p_{nw}, S_w)_{i,j,k}$ is a solution at the block (i, j, k), p_{nw} and S_w are non-wetting pressure and wetting saturation, respectively. Then, Eqs. 7 and 8 then can be rewritten into the form:

$$\{F(\mathbf{X}_{i,j,k})\}^{n+1} = \{f(\mathbf{X}_{i,j,k})\}^{n+1} - \{h(\mathbf{X}_{i,j,k})\}^{n+1} + \{h(\mathbf{X}_{i,j,k})\}^{n} + Q_{i,j,k}^{n+1} = 0 \tag{9}$$

We thus have a system of $N_x \cdot N_y \cdot N_z$ equations with $N_x \cdot N_y \cdot N_z$ unknowns, $\mathbf{X}_{i,j,k}$. Finite difference methods generally yield a sparse matrix which allows special matrix solution methods to be used. The structure of the resulting coefficient matrix has a 'block' triangular form shown in Fig. 6. The matrix of order $N = N_x \cdot N_y \cdot N_z$ can be partitioned into $N_z \cdot N_z$ submatrices. Each submatrix can be further partitioned into $N_y \cdot N_y$ submatrices, where each submatrix is of order $N_x \cdot N_x$. For one-dimensional problems, SENDRA uses the Thomas algorithm to solve the block system equations. For two-dimensional problems, a sparse matrix technique (Aziz and Settari 1979) is used to solve the equations. In addition, the technique of D4 ordering (Aziz and Settari 1979) is applied in two-dimensional problems. The D4 technique provides the greatest advantage (Aziz and Settari 1979) for two-dimensional reservoir simulation, especially for complex reservoir shapes. But our problem is the three-dimensional simulation for fluid flow through a sample which has a regular shape. We need to find a matrix solver to deal with the matrix equation which is yielded by the three-dimensional problem.

For the simulation involving many grid points, direct methods are too expensive to be practical, so iterative methods are good choices (Peaceman 1977). SPLIB is a library of sparse iterative solvers, with preconditioners, for rapid prototyping of solvers for nonsymmetric linear systems of equations (Bramley and Wang 1995). The data structure of the coefficient matrix used in SPLIB is CSR, compressed sparse row. This is the transpose of the data structure used for the Harwell/Boeing collection of matrices. Harwell/Boeing format can store the nonzeros of the matrix in an efficient way. Though SENDRA can only create the matrix in IJ-value format (also called coordinated format) (Alvarado 1993), a routine is supplied by an important package, SPARSKIT, which creates a Harwell/Boeing (H/B) file from a matrix in any format (Saad 1994). After the IJ-value format is converted into H/B format by implementing SPARSKIT, SPLIB provides us a fast and accurate solution method for the type of linear systems encountered in SENDRA.

3.3 SENDRA 3D Test

In multiphase flow, 2D SENDRA represents two spatial coordinate directions only. We extended the code to include all three spatial coordinate directions in order to account for spatial variations in the

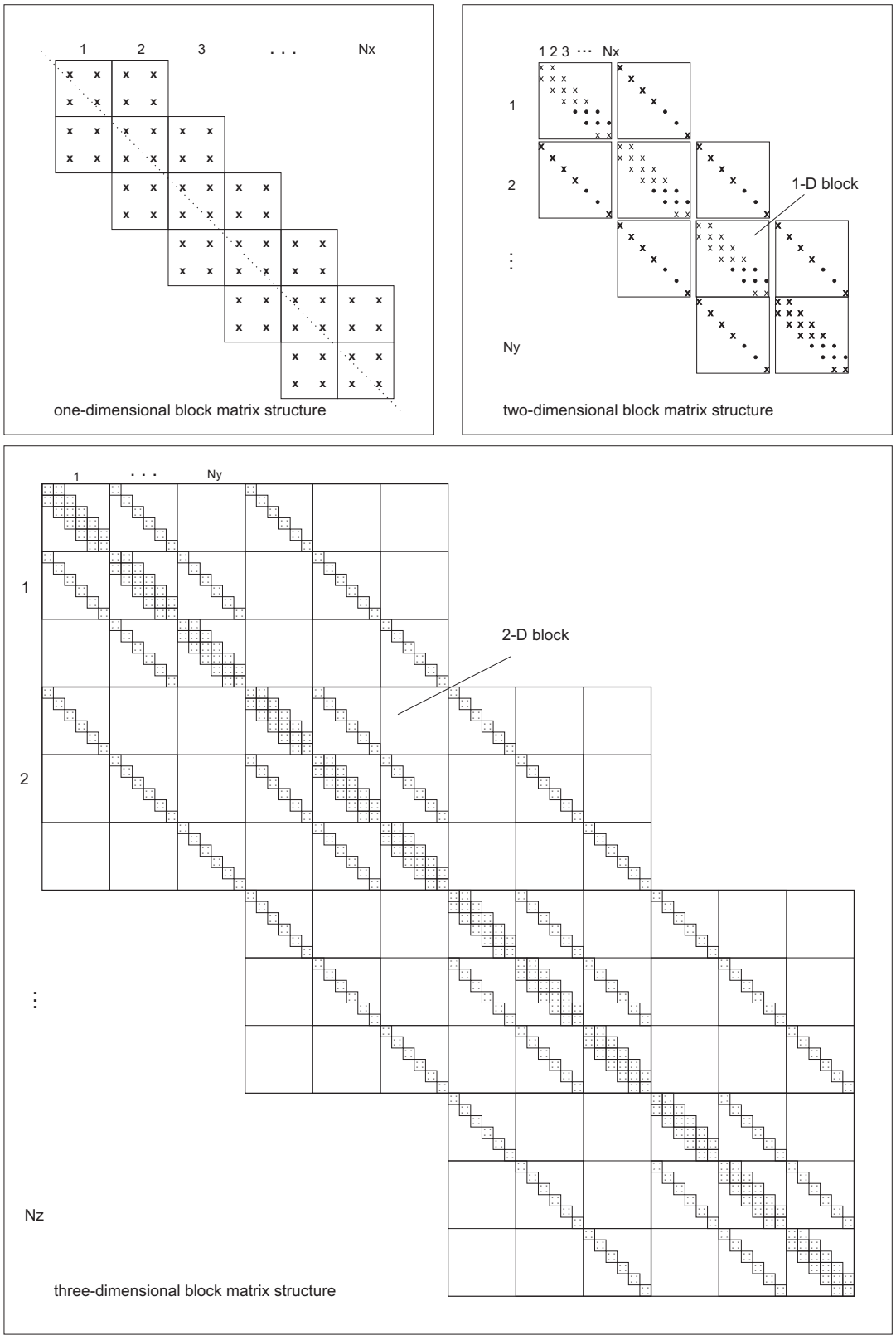

Figure 6: The block matrix structure

porosity and absolute permeability. The validity of SENDRA has been verified for two-dimensional (2D) representations. The aim of this section is to demonstrate the validity of simulating fluid flow with three-dimensional (3D) representations.

After extending SENDRA from 2D to 3D and compiling on our Linux workstation, the modified program needs to be tested and validated with the original 2D SENDRA program. For the sake of the validation, we take the x-direction horizontal, two-dimensional flow as a test case to validate the extended code. In Fig. 7, the left image presents a grid system with 10 blocks in the x-direction, 5 blocks in the y-direction, and 1 block in the z-direction (as a vertical plane). The right image presents another grid system with 10 blocks in the x-direction, 1 block in the y-direction and 5 blocks in the z-direction (as a horizontal plane). The rock properties (porosity and permeability) which are assigned to different blocks should satisfy the following relationship:

$$K_V(i,j,1) = K_H(i,1,j)$$
$$\phi_V(i,j,1) = \phi_H(i,1,j)$$

The subscripts H and V represent the horizontal and vertical plane, respectively. Multiphase flow through the vertical plane is simulated by the original 2D SENDRA code, and flow through the horizontal plane is simulated by the three-dimensional SENDRA code with only a single layer of grid blocks in the y-direction. The data listed in Table 1 and the flow functions are then implemented in SENDRA to simulate a displacement experiment. If gravity is neglected (g=0), the 2-dimensional horizontal plane should have the same results as the 2-dimensional vertical plane.

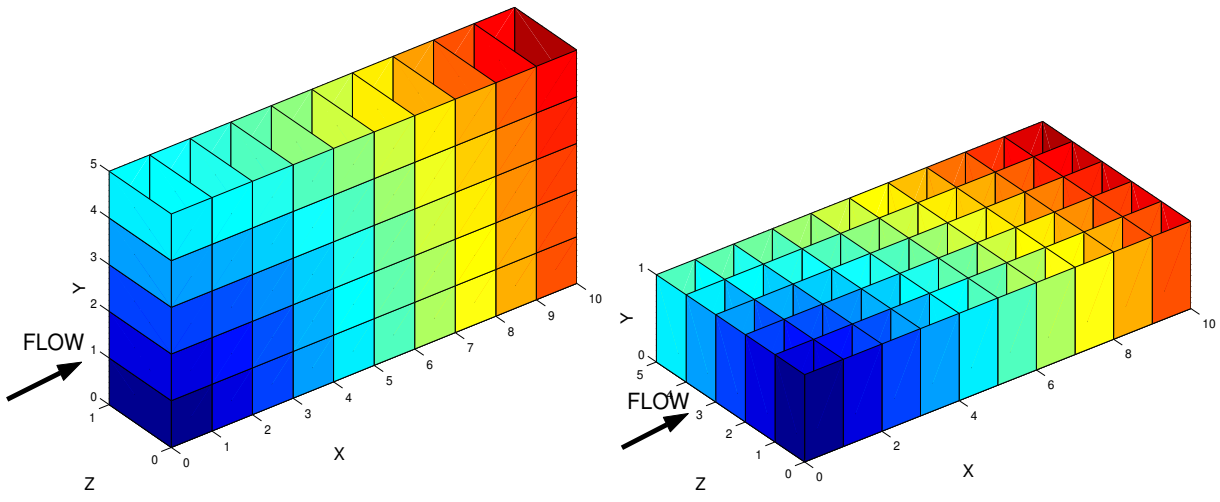

Figure 7: 2-dimensional vertical plane (left); 2-dimensional horizontal plane (right)

Table 1: The SENDRA input for horizontal and vertical planes

Core Properties		
	Vertical Plane	Horizontal Plane
Porosity [%]	20	20
Permeability[mD]	1,000, 900, 800, 700, 600	1,000, 900, 800, 700, 600
Core length(x-direction) [mm]	40	40
Core height(y-direction) [mm]	40	10
Core width(z-direction) [mm]	10	40
Fluid Properties		
Oil Viscosity [cP]	0.75	0.75
Water Viscosity [cP]	0.339	0.339
Oil Density [kg/m^3]	800	800
Water Density [kg/m^3]	1,000	1,000
Data Defining Initial State		
Pressure [kPa]	33,500	33,500
Water Saturation [frac]	0.2	0.2
Oil Saturation [frac]	0.8	0.8
Grid Data		
No. of Grid Blocks in x-direction	10	10
No. of Grid Blocks in y-direction	5	1
No. of Grid Blocks in z-direction	1	5
Two-Phase Experiment		
Oil Injection Rates [ml/min]	0.0, 0.0	0.0, 0.0
Water Injection Rates [ml/min]	1.0, 5.0	1.0, 5.0
Corresponding Injection Times [min]	1,000, 1,500	1,000, 1,500
Total Experimental Time [min]	2,000	2,000

We compared results for fluid flow through the 2D horizontal plane and vertical plane. The simulated water saturation profiles, oil production, and differential pressure are found to be in good agreement, providing a validation for the computer code extension. The results of two simulations are shown in Figs. 8, 9, and 10.

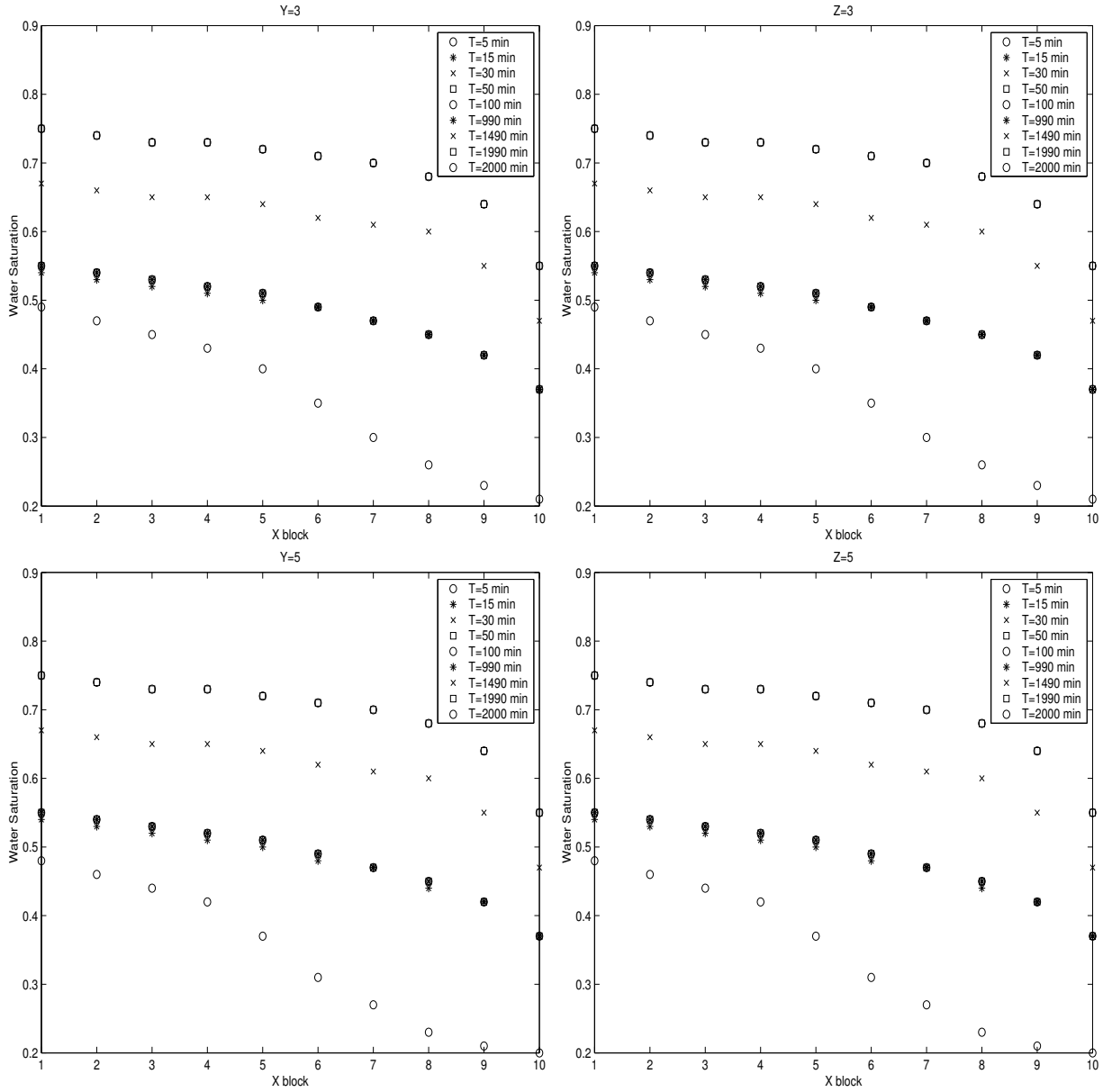

Figure 8: Water saturation profiles for the two planes. 2-dimensional horizontal plane (left), 2-dimensional vertical plane (right)

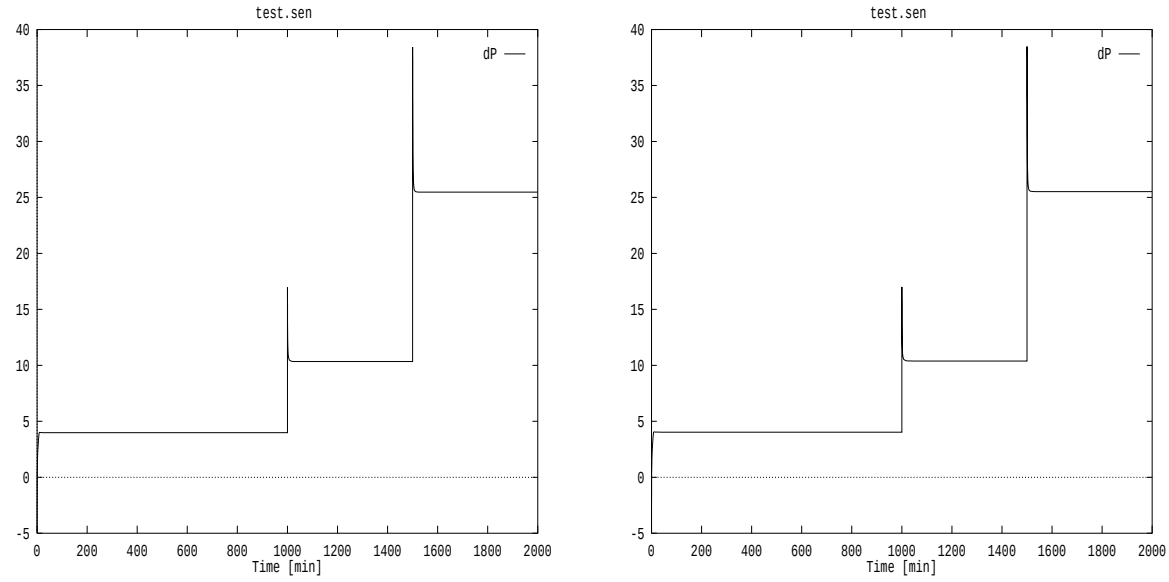

Figure 9: Pressure drop for the two planes. 2-dimensional horizontal plane (left), 2-dimensional vertical plane (right)

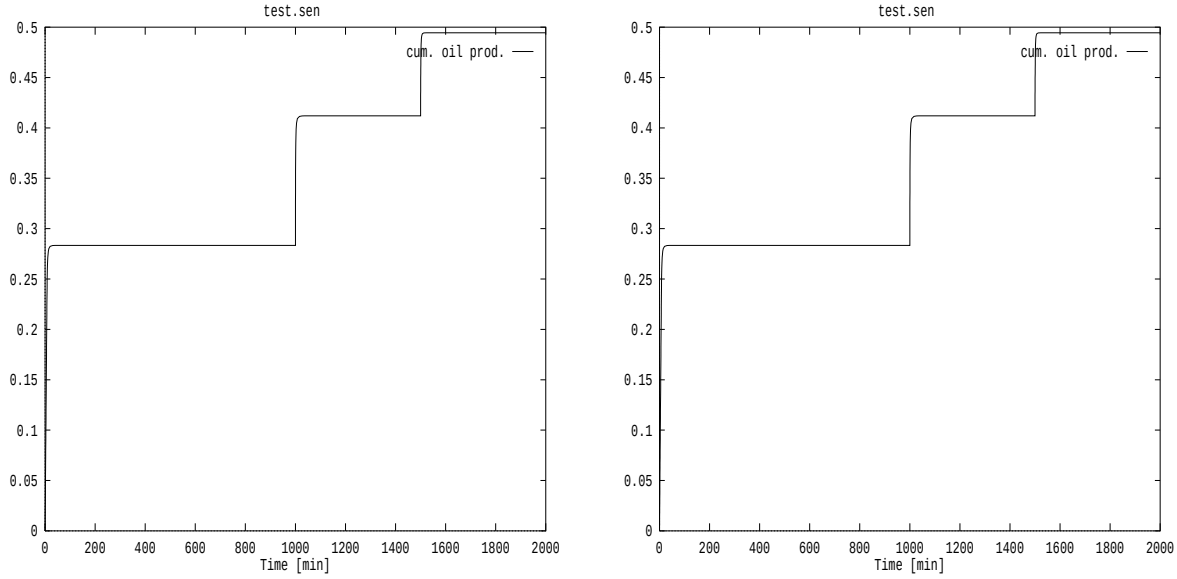

Figure 10: Oil production for the two planes. 2-dimensional horizontal plane (left), 2-dimensional vertical plane (right)

3.4 Two-Phase Flow Experiment and Three Dimensional Simulation

SENDRA contains associated software to estimate relative permeability and capillary pressure curves from measured data. Here, we demonstrate this process with the three-dimensional implementation discussed previously.

Two-Phase Flow Experiment

A multirate primary drainage experiment was performed on a composite core sample. The sample and fluid properties used to simulate the experiment are listed in Table 2. Four successive injection rates, each to be held for 80 minutes, were chosen. Pressure-drop across the sample and water production were monitored during the displacement experiment. Further details can be found elsewhere (Phan *et al.* 2001).

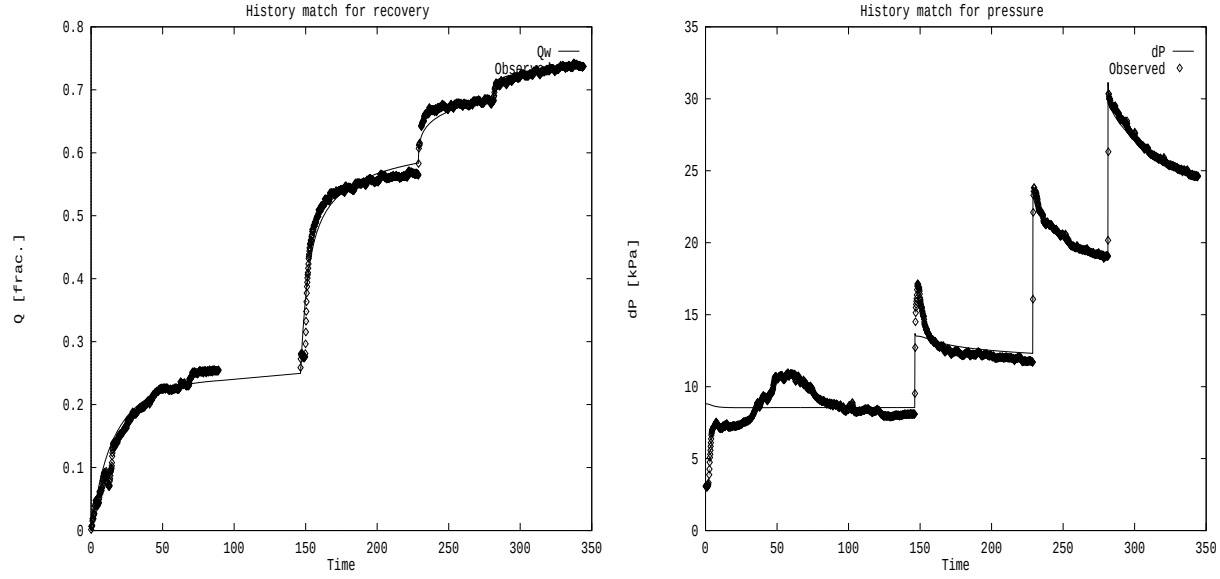

Figure 11: Predicted and measured water production data (left); calculated and measured pressure drop data (right) in the multirate two-phase experiment

Three-Dimensional Simulator Results

The parameter estimation package of SENDRA systematically adjusts the flow properties (Watson *et al.* 1988) so that the simulated values (e.g., differential pressure and production) match the experimental data which were recorded in the two-phase flow experiment. Figures 11 and 12 show

Table 2: Core flood simulator input

Core Properties	
Porosity [%]	22
Permeability[mD]	1351.9, 1264.3
Core length(x-direction) [mm]	47.1
Core height(y-direction) [mm]	25
Core width(z-direction) [mm]	10
Fluid Properties	
Oil Viscosity [cP]	1.125
Water Viscosity [cP]	1.0
Oil Density [kg/m^3]	750
Water Density [kg/m^3]	1,000
Data Defining Initial State	
Pressure [kPa]	101.3
Water Saturation [frac]	1.0
Oil Saturation [frac]	0
Grid Data	
No. of Grid Blocks in x-direction	40
No. of Grid Blocks in y-direction	3
No. of Grid Blocks in z-direction	3
Two-Phase Experiment	
Oil Injection Rates [ml/min]	0.04, 0.3, 1, 2
Water Injection Rates [ml/min]	0, 0, 0, 0
Corresponding Injection Times [sec]	8777, 4950, 3150, 3780
Total Experimental Time [sec]	20657

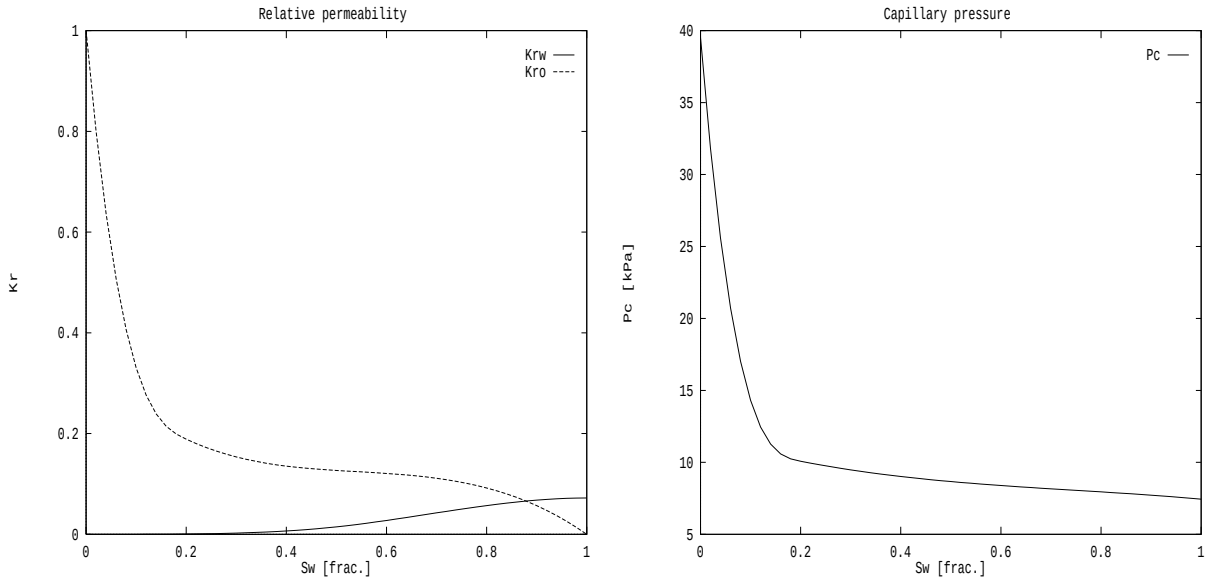

Figure 12: Estimated relative permeability (left) and capillary pressure (right)

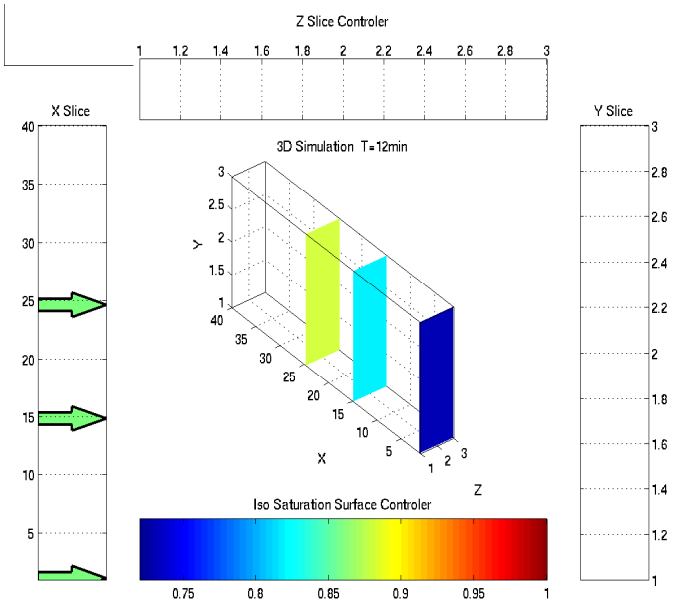

Figure 13: Water saturation distribution in planes X=1, X=15 and X=25

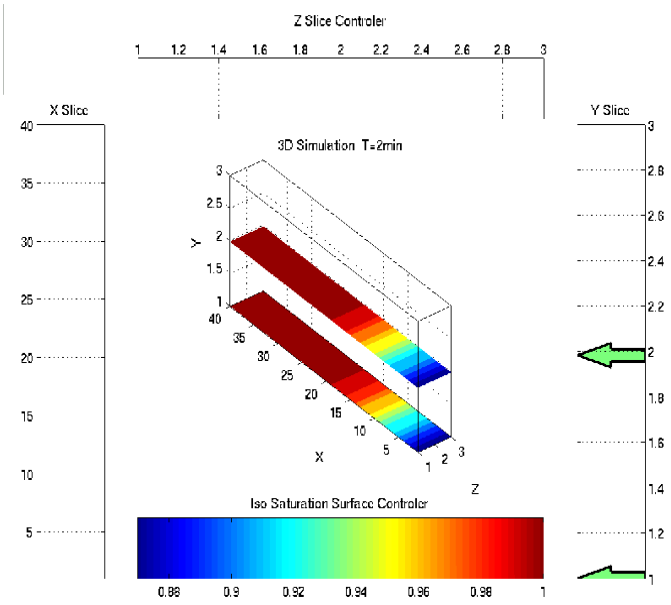

Figure 14: Water saturation distribution in planes Y=1 and Y=2

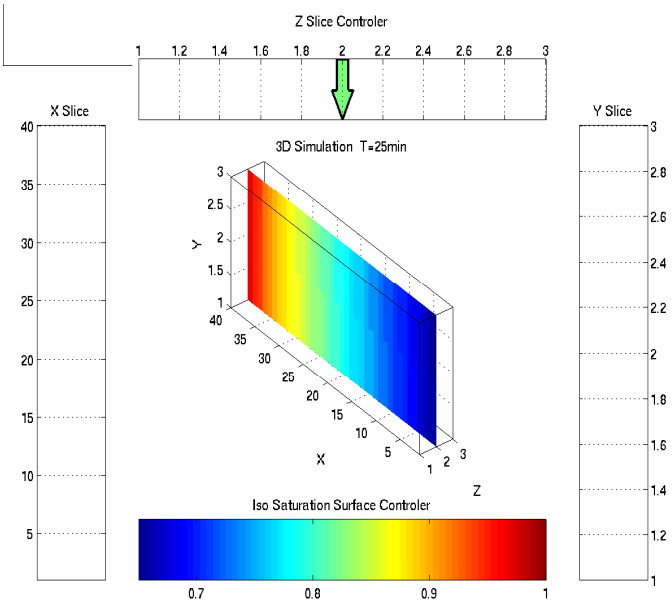

Figure 15: Water saturation distribution in plane Z=2

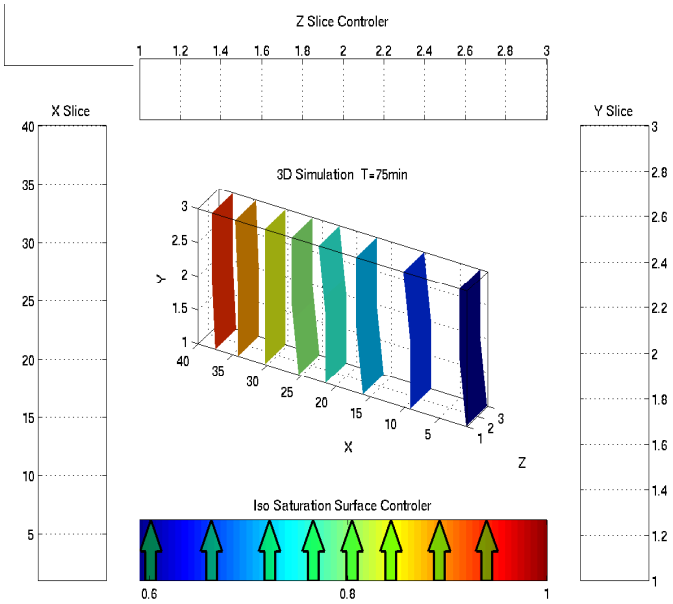

Figure 16: Water iso-saturation surface in the sample

the measured data with the corresponding simulated values. The corresponding estimates of the relative permeability and capillary pressures curves are provided in Fig. 12.

The general trends of the data are represented by the simulations. However, the precision of the match is not as great as we normally expect. This is attributed to some physical features not being adequately represented by the simulation, although experimental error has not entirely been ruled out for this data set. In particular, we cannot explain the "hump" in the pressure drop measurements during the first set flow rate (from 0 to 150 minutes).

The mismatch could be the result of an inadequate representation of spatial variations in porosity and permeability. In this simulation, we represented the properties as being different in three spatial regions - one for each of the two sample sections, and one for the composite joining surface. We did not perform the experiments to determine the actual distributions of the porosity and permeability. In the future, we will determine those properties so that we can adequately account for spatial variations in the simulations. Here, the objective of demonstrating the estimation of multiphase flow properties with three-dimensional simulations was met.

Further modifications are required to conveneiently represent the solutions from the three-dimensional simulations. We are evaluating exprting data from SENDRA to other software programs, such as MATLAB, for graphical representation. The water saturation profiles are shown in Figs. 13-16. The green arrows in the top, right and left white bar give the positions of the X, Y,

Z slices. The different colors in the slices are assigned by the different saturation values indicated in color bar at the bottom. The values of the iso-saturation surfaces shown in Fig.16 are indicated by the green arrows in the color bar.

4 Identifiability Study for Permeability Estimation

4.1 Introduction

In this project, we are developing a reliable method to estimate absolute permeability distributions within heterogeneous porous media (Chang *et al.* 2000; Hollenshead *et al.* 2001). We obtain the fluid flow velocity field inside porous media using NMR velocity imaging experiments, and the permeability distribution is found by solving an inverse problem. In our approach, we have used regularization because the problem tends to be ill-conditioned, which means that small changes or errors in the data can seriously affect the solution. The use of regularization imposes *a priori* knowledge, such as the expectation of the unknown property is smooth, on the estimation problem. Thus, if the solution is not identifiable, *i.e.*, it cannot be determined uniquely on the basis of the measured data, we will find the smoothest estimate that is consistent with the measured data.

Seto (1999) presented two specific pathological cases of permeability estimation problems as illustrated in Fig. 17. The gray and white areas of the two experiments show different permeability

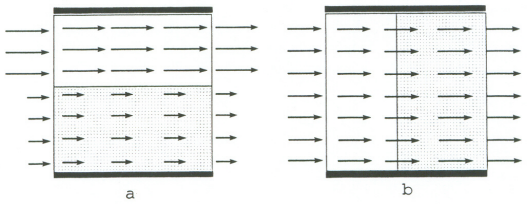

Figure 17: Velocity vector fields for pathological cases (Seto 1999)

fields. For the case represented by Fig. 17a, for which the heterogeneity is parallel to the flow, the permeability distribution is identifiable on the basis of velocity data alone. Thus, in this case, the permeability field can be completely constructed by using only the velocity data. For the case represented by Fig. 17b, for which the heterogeneity is perpendicular to the flow field, the permeability is not identifiable. As apparent in the figure, the velocity distribution data does not depend on the values of the permeability, and consequently that data provides no information

about the permeability distribution. Therefore, it is impossible to properly construct permeability without any additional information.

Seto (1999) considered other experimental designs whereby transverse pressures on the periphery of the sample are measured in addition to the velocity distributions. An *experimental design* is the protocol by which the experiment is conducted and data are measured. Besides these pathological cases, he simulated similar situations represented by varying permeability contact line at different angle positions. His results show that we get better estimates of permeability as we add more pressure data.

When it comes to implementation, however, it is not easy to measure transverse pressure data, even at a few points, because the experiment should be performed inside a small probe coil in the NMR bore. In this reporting period, we explored alternative experimental designs, which are more easily implemented to obtain improved estimation of permeability distributions.

4.2 Experimental Designs and Numerical Simulation

In the new experimental designs, multiple velocity fields obtained in different experiments are used together to estimate the permeability distribution of each sample. Previously, we used a single experiment, which represented a single velocity field. We obtain different velocity fields by repeating flow experiments with the same sample, but changing the boundary conditions and position of entering flow, as described in the following.

The new experimental designs are illustrated in Fig. 18. The arrows represent fluid flows which enter into and exit from the sample through the interfaces (thin lines). The thick lines around the sample indicate boundaries where the flow cannot penetrate. Experiment A is the case that has been typically used in our previous analysis. There are obviously a large number of other possibilities of experimental designs depending on the ways of blocking the flow and selecting the entering positions. Any combination of those can be used together for solving the inverse problem, once we are able to simulate the flow for each case. It is expected that we will have better estimates as we have more sets of velocity fields.

The permeability estimation problem is expressed formally as a minimization problem with respect to permeability $\mathbf{k}$:

$$\min_{(\mathbf{k})} J = J_{expt} + \lambda J_{reg} \tag{10}$$

Here, J is the objective function which consists of the data fitting term, J_{expt}, and the regularization term, J_{reg}. λ is the regularization parameter. For each experiment of Fig. 18, the data fitting term

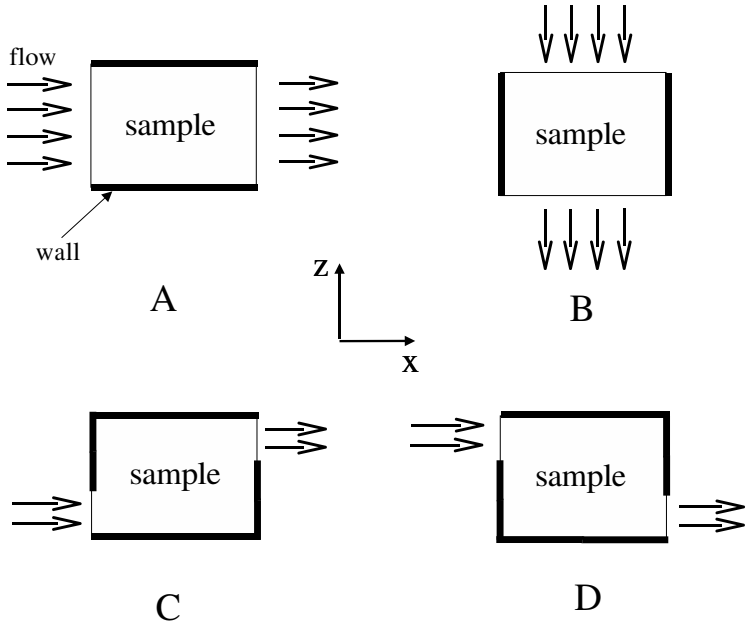

Figure 18: Examples of experimental designs

takes the following form

$$J_{expt,\Gamma} = \frac{1}{2}\sum_{i}^{N_v}(\mathbf{v}_{i,\Gamma}^{obs} - \mathbf{v}_{i,\Gamma}^{calc})^2, \qquad \Gamma \in \{\text{A, B, C, D}\} \tag{11}$$

Here, $\mathbf{v}$ is velocity vector, N_v is the number of positions where velocity data are acquired, and superscripts *obs* and *calc* indicate experimentally observed and calculated values, respectively. Subscript Γ represents one of the experimental designs of A, B, C and D, which indicates that the experimental velocity fields and the estimated values should be obtained and calculated in different ways that are associated with the boundary conditions of each particular experiment. In Eq. 11, the contribution from pressure data and the weighting term are omitted because we do not use transverse pressure data here and all the velocity data are weighted in the same way.

In our numerical simulation, the boundary conditions are chosen as

$$\begin{aligned} &p = p_{ent} && \text{at entering positions of fluid} \\ &p = p_{out} && \text{at exiting positions of fluid} \\ &\mathbf{v}\cdot\mathbf{n} = 0 && \text{at non-penetrating walls (thick lines in Fig. 18),} \end{aligned} \tag{12}$$

where p is pressure and $\mathbf{n}$ indicates the normal vector at the boundaries. In order to use multiple velocity fields together, the data fitting term needs to be written as

$$J_{expt} = \sum_{\Gamma} J_{expt,\Gamma} \tag{13}$$

In this work, combinations of experiments A and B (experiment A + B) and experiments C and D (experiment C + D) are tested and evaluated with simulated data. The objective functions for the two cases are given by

$$\begin{aligned} J_{A+B} &= J_{expt,A} + J_{expt,B} + \lambda J_{reg} \\ \text{and} \quad J_{C+D} &= J_{expt,C} + J_{expt,D} + \lambda J_{reg} \end{aligned} \tag{14}$$

We took a square sample for experiment A + B, and a rectangular sample with 2:1 side ratio for experiment C + D. For experiment C or D, one fourth of the entering and exiting surface is allowed for fluid to flow through and the other portions are blocked. After a "true" permeability field is specified, velocity "data" are generated with a two-dimensional simulation code. Then the permeability is estimated, using the previously developed code for permeability estimation (Seto *et al.* 2001), and compared with the known true values. We modified the code by changing boundary conditions and combining data fitting terms of different experimental designs.

4.3 Results and Discussion

Experiment A + B with square sample

We first tried to estimate a simple permeability distribution of a square sample by experiment A + B (Fig. 19). The true permeability in Fig. 19 has a distorted discontinuity line and can be considered as a variation of the pathological case discussed before. With experiment A, where the major part of the discontinuity line is parallel to the flow, the estimated permeability is relatively close to the true values although it has a small step at the distorted discontinuity line. However, with experiment B, where the major part of the discontinuity line is perpendicular to the flow, the permeability in the down-stream region is not correctly estimated. This failure is due to the fact that experiment B is closer to the unidentifiable case than experiment A. The last graph in Fig. 19 clearly shows that we have improved estimation of the permeability field by combining results of the two experiments.

The analysis of experiment A + B is continued with another permeability distribution (Fig. 20). A smoothly varying property is chosen by generating randomly a set of coefficients for a B-spline representation of the permeability. It is instructive to investigate each A and B experiment independently before testing experiment A + B. Figures 21 and 22 show that, with different positions of entering flow, each experiment generates a little different estimation of the permeability distributions. They are not far from the true permeability of Fig. 20, but there are some discrepancies. On

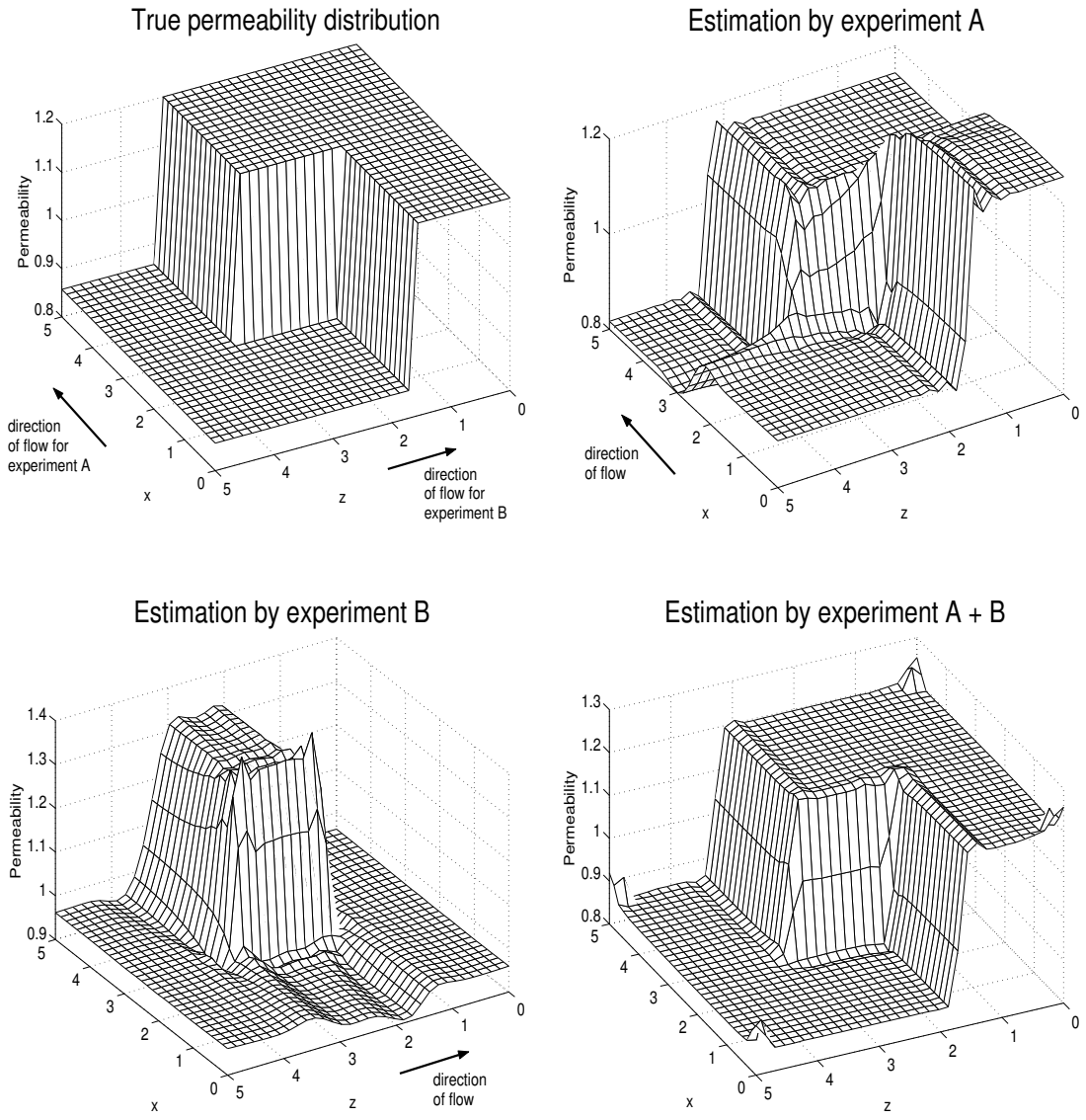

Figure 19: Increase of identifiability by applying two experiments (A and B) together

the other hand, experiment A + B, where both velocity fields are used, gives a very close estimation to the true distribution as shown in Fig. 23.

Root-mean-squared errors (RMSE) of velocity and permeability show this result clearly. In Table 3, RMSE of velocity and permeability are defined as

$$\mathrm{RMSE}[\mathbf{v}] = \sqrt{\sum_{i}^{N_v} \frac{(v_{x,i}^{obs} - v_{x,i}^{calc})^2 + (v_{z,i}^{obs} - v_{z,i}^{calc})^2}{N_v}} \quad \text{and} \quad \mathrm{RMSE}[k] = \sqrt{\sum_{i}^{N_k} \frac{(k_i^{true} - k_i^{calc})^2}{N_k}}, \quad (15)$$

where N_k is the number of grid points where the permeability is evaluated. k is expressed as a scalar, assuming that it is isotropic. The average magnitude of experimentally measured velocities

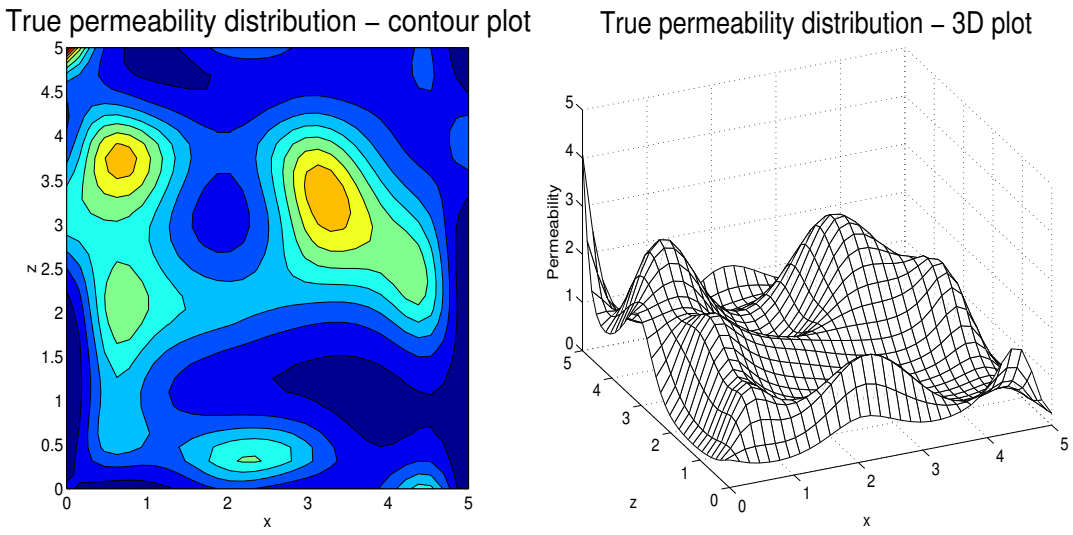

Figure 20: True permeability distribution of square sample

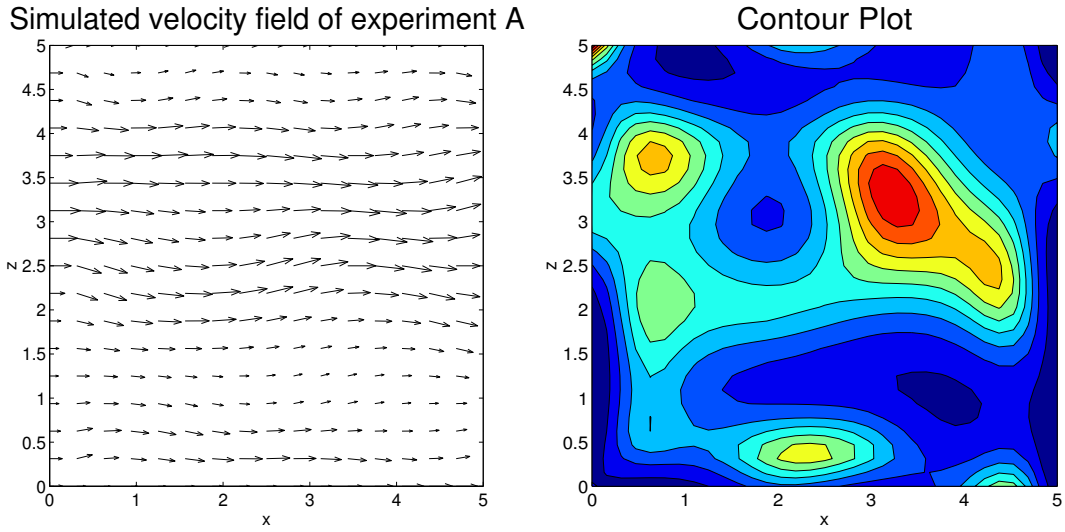

Figure 21: Estimation by experiment A with square sample

$< v^{obs} >$ and average true permeability $< k^{true} >$ are calculated by

$$< v^{obs} >= \sqrt{\sum_{i}^{N_v} \frac{(v_{x,i}^{obs} + v_{z,i}^{obs})^2}{N_v}} \quad \text{and} \quad < k^{true} >= \frac{1}{\sum_{i}^{N_k} (1/k_i^{true})} \tag{16}$$

and presented in the table. Table 3 shows that RMSE of both velocity and permeability are significantly reduced by using the experiments A and B together. The reduction of RMSE of permeability is remarkable. Compared with either case using only one set of the velocity fields, the

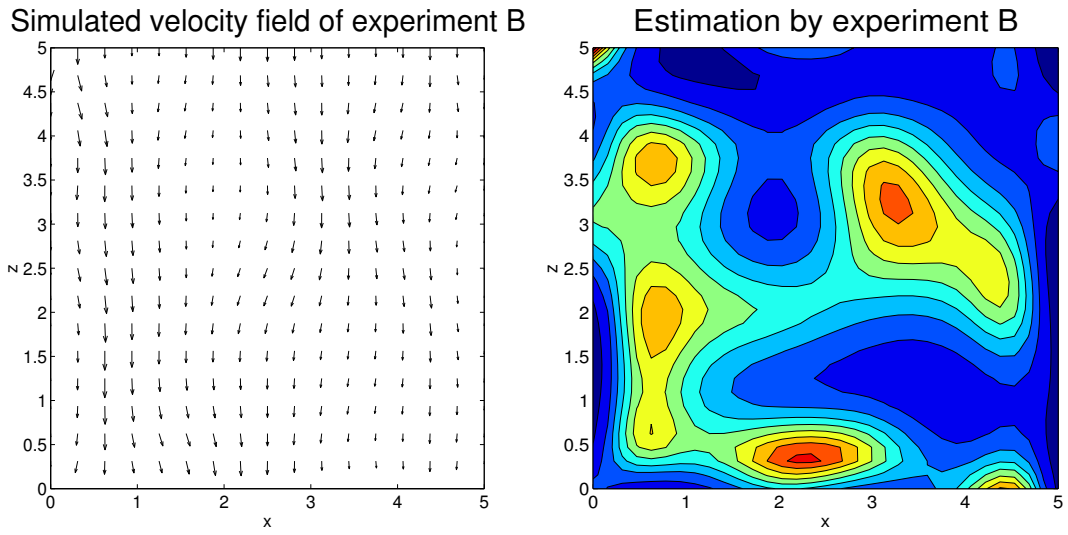

Figure 22: Estimation by experiment B with square sample

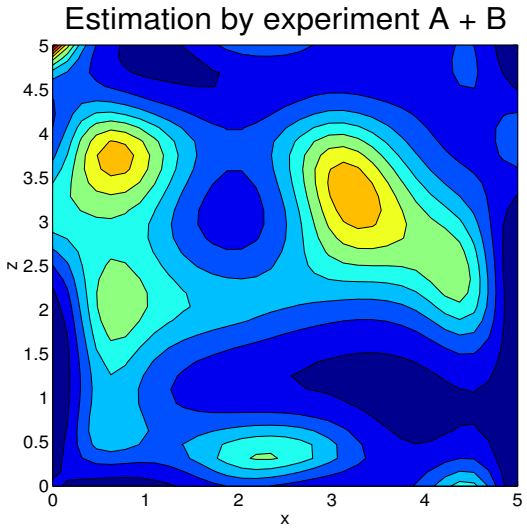

Figure 23: Estimation by experiment A + B with square sample

experiment A + B gives a four order magnitude reduction in the permeability RMSE.

Experiment C + D with rectangular sample

A true permeability field for a rectangular sample with 2:1 side ratio is chosen in the same way as experiment A + B, and it is shown in Fig. 24. Before testing experiment C + D, independent analyses with experiments A, C and D are performed for the purpose of comparisons. The

experiment design	RMSE[v]	$< v^{obs} >$	N_v	RMSE[k]	$< k^{true} >$	N_k
A	0.0007160	0.8472	289	0.1292	0.8408	1089
B	0.0006893	0.8309	289	0.2501	0.8408	1089
A + B	0.00001453	0.8391	578	0.00002178	0.8408	1089

Table 3: RMSE of experiments with square sample

simulated velocity data of Figs. 25, 26 and 27 illustrate the behavior of fluid flow corresponding to each experimental design. The overall shapes of the estimated permeability fields by the three independent experiments are all similar to the true one, but there are discrepancies. Again, the combined experiment C + D (Fig. 28) gives a much better estimation.

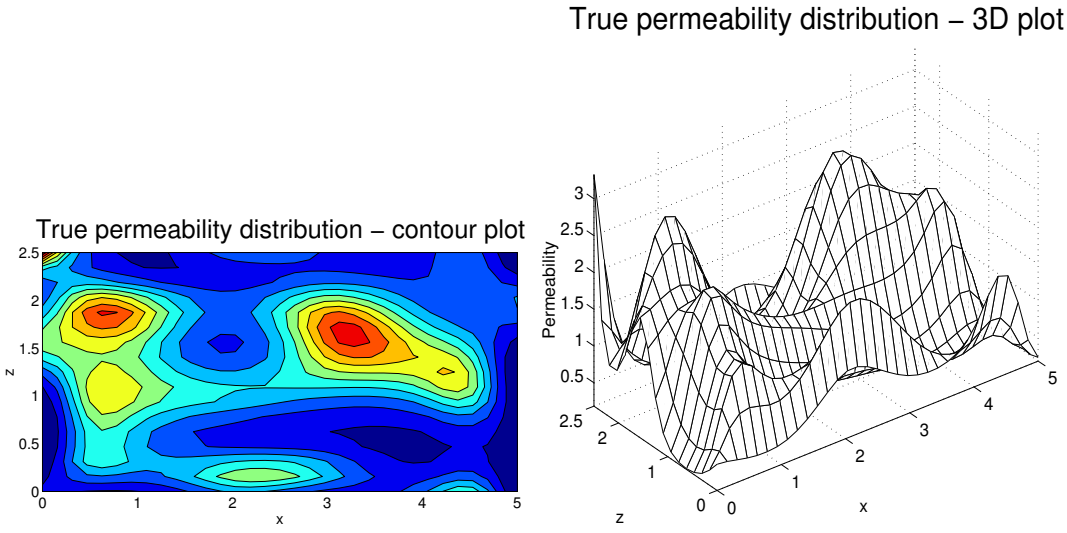

Figure 24: True permeability distribution of rectangular sample

experiment design	RMSE[v]	$< v^{obs} >$	N_v	RMSE[k]	$< k^{true} >$	N_k
A	0.0004576	0.8592	153	0.07216	0.8344	561
C	0.01049	0.6104	141	0.7685	0.8344	561
D	0.0009569	0.6343	141	0.1267	0.8344	561
C + D	0.00001512	0.6010	306	0.0006260	0.8344	561

Table 4: RMSE of experiments with rectangular sample

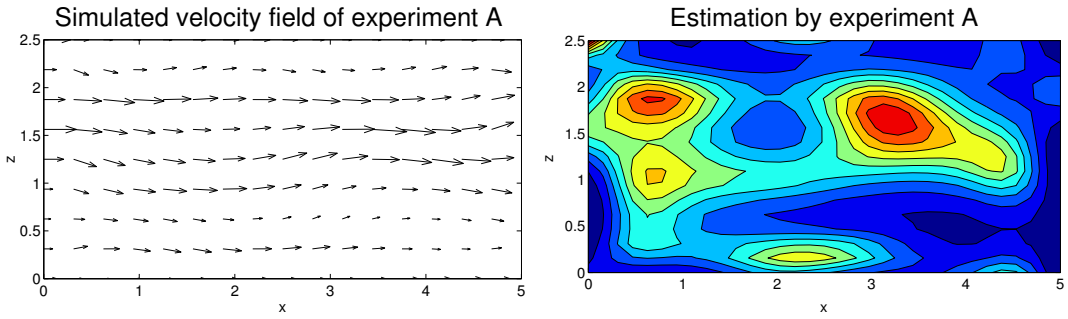

Figure 25: Estimation by experiment A with rectangular sample

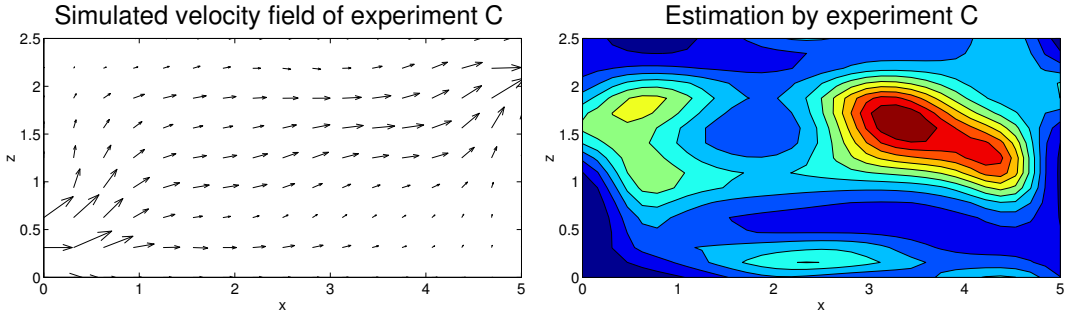

Figure 26: Estimation by experiment C with rectangular sample

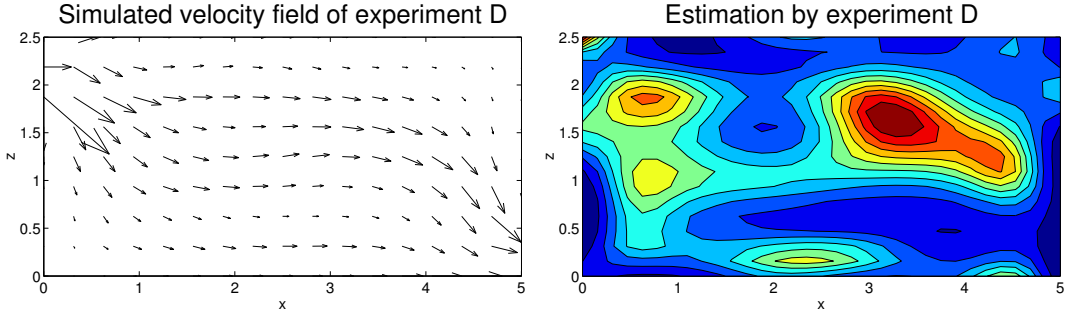

Figure 27: Estimation by experiment D with rectangular sample

Table 4 summarizes RMSE values of velocity and permeability. Compared with experiment A, C or D, C + D has significantly reduced RMSE of both velocity and permeability.

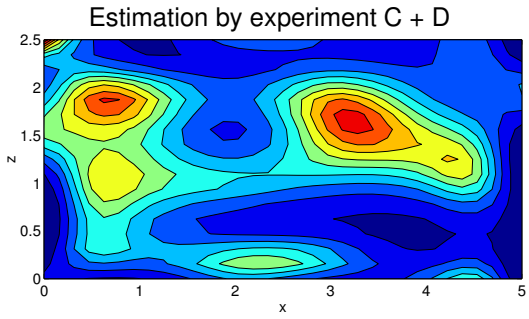

Figure 28: Estimation by experiment C + D with rectangular sample

5 Experimental Apparatus

The project requires the construction and use of several key pieces of experimental equipment. These include the apparatus (Chang *et al.* 1999) for general flow experiments in the NMR imager, the positioner and corresponding sample holder (Hollenshead *et al.* 2001) for experiments in determining the three-dimensional porosity and saturation (Phan *et al.* 2001), and the production device (Phan *et al.* 2001) for experiments in determining water production in two-phase experiments (Phan *et al.* 2001). In this reporting period, work has been directed to the design and construction of apparatus to implement our new experimental designs to estimate permeability distributions.

5.1 Preparation of Samples

We have custom-built a device to accurately cut rock samples for our experiments. This device is shown in Fig. 29.

5.2 Experiment Design

In order to perform experiments to estimate the permeability distribution as described in section 4, the following requirements must be met:

1. The experiments for flow through two sides are performed on the same sample, as shown in Fig. 31. These experiments will provide two sets of the experimental data for simulation in two cases, in which the rock properties are identical.

2. The sample should occupy the same position in the NMR imager when different experiments are performed.

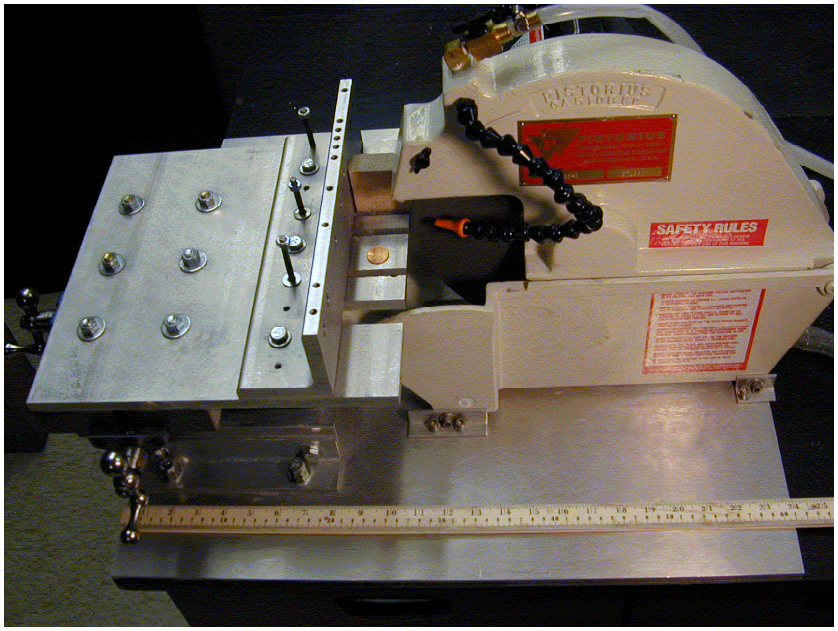

Figure 29: The custom-built machine for cutting rock sample

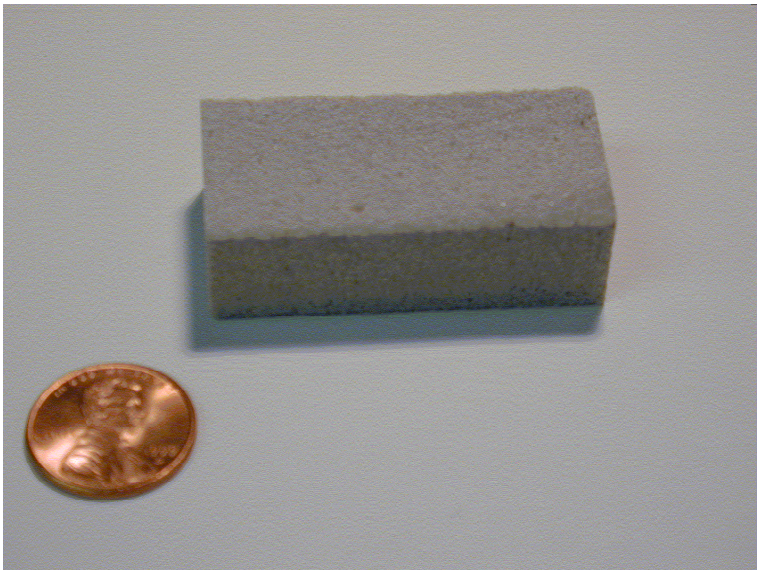

Figure 30: Rock Sample (15mm $\times$ 23mm $\times$ 48mm)

3. The surfaces of the sample should be not damaged in any experiment. In other words, the sample properties should not change in different experiments.

4. The material of the sample holder must be non-magnetic to place inside the NMR imager.

Each requirement is satisfied through the design and the construction of the sample holders. To satisfy the first requirement, we will perform two experiments for each sample, in which fluid flows through each side in each experiment (Fig. 31). To satisfy the second requirement, the sample and sample holder will be set at the same position in NMR imager by aligning a mark on the sample holder, a mark on the birdcage-coil, and a mark on the NMR imager. This method was successful when performed in experiments to determine the three-dimensional porosity and saturation distributions (Phan *et al.* 2001). To satisfy the third requirement, we made four separate pieces to hold the sample before assembling them into the cylinder holder (Fig. 32). After the completion of one experiment (Fig. 31a), we will disassemble and reassemble them into another sample holder (Fig. 33) to perform the next experiment (Fig. 31b). To satisfy the fourth requirement, all parts of sample holder are made of plexiglass, and all bolts are nylon.

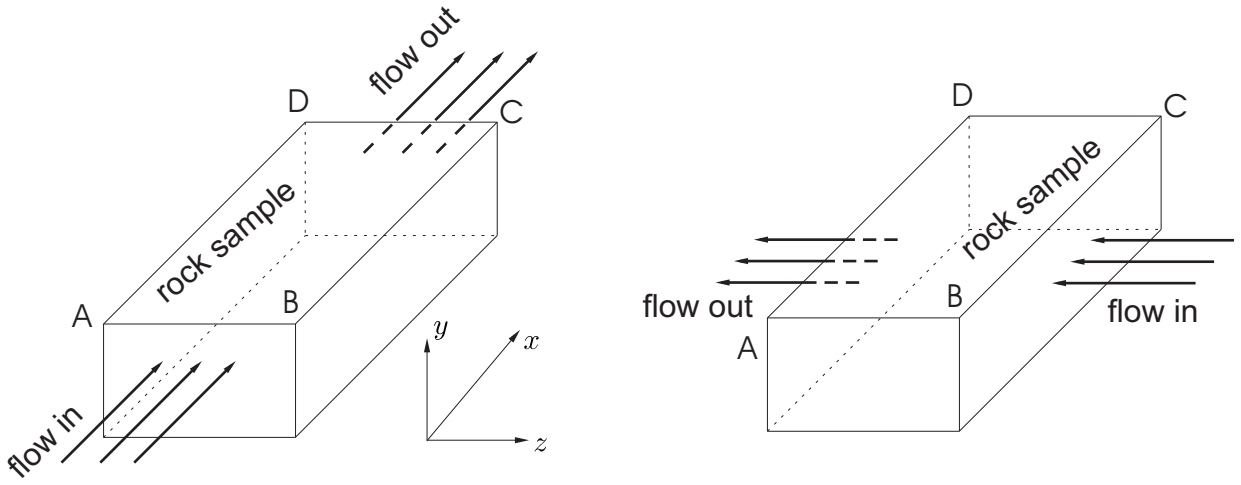

(a) Experiment A, fluid flows in x direction

(b) Experiment B, fluid flows in z direction

Figure 31: Experiments for estimation of permeability distribution

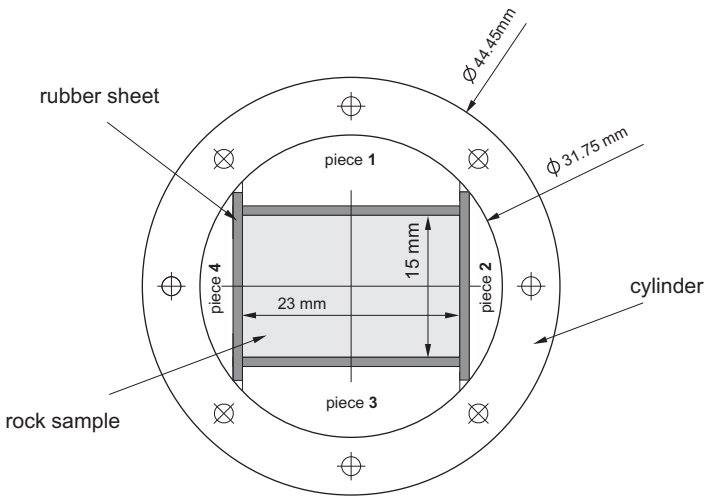

Figure 32: Assembly of sample holder and rock for experiment A (inlet and outlet are in the caps)

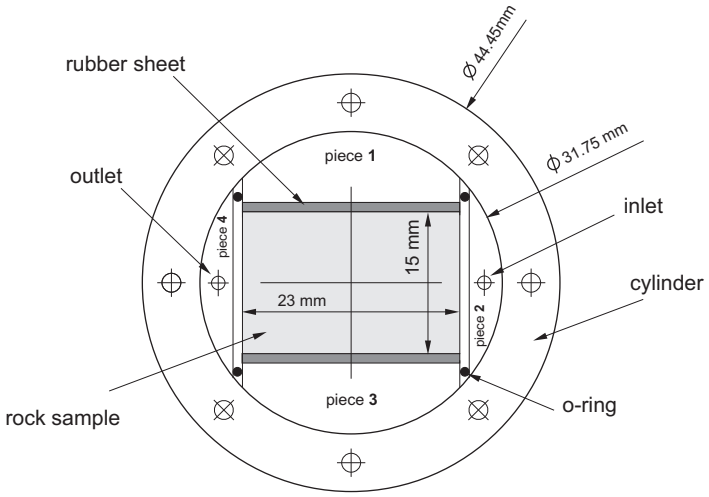

Figure 33: Assembly of sample holder and rock for experiment B (inlet and outlet are in piece 2 and piece 4)

5.3 Progress of experiments

In this reporting period, we have finished making rock samples and the sample holder for one experiment (Fig. 34). The other sample holder (Fig. 33) for use with experiments as shown in Fig. 31a and Fig. 31b, will be finished directly.

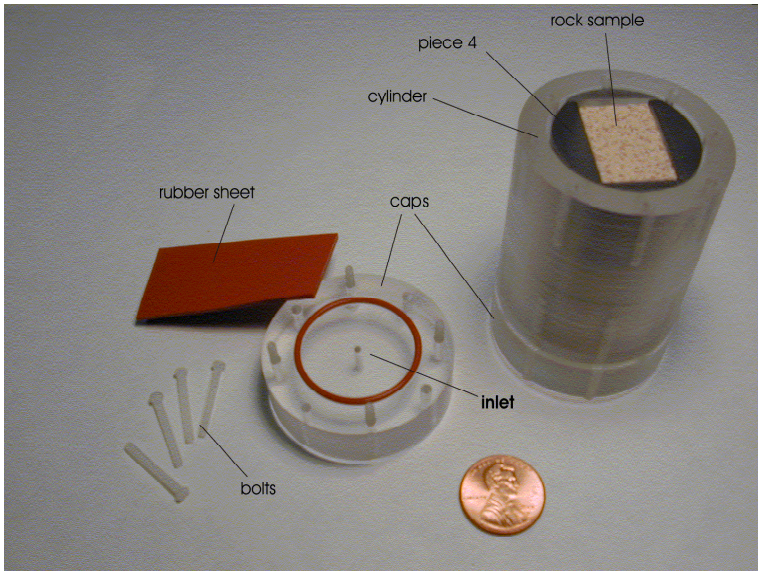

Figure 34: Sample holder and rock in experiment A

6 Conclusions

The overall objective of this research project is to develop various unique capabilities of NMR imaging and spectroscopic techniques for probing macroscopic properties important for describing the flow of one or more fluid phases in heterogeneous media. During this reporting period, the laboratory site for our new MRI equipment was completed. The MRI has been delivered and is currently being installed.

We extended the computer code, SENDRA, so that all three spatial coordinate directions can be represented when simulating laboratory displacement experiments. We validated the code, and demonstrated its use by estimating multiphase flow functions from experimental data.

We presented new experimental designs to develop a more reliable method to estimate permeability distributions. The performance of the new method is evaluated with numerical simulations of some examples. We observed from the results that better estimation is obtained by combining independent flow experiments and using them together in the permeability estimation process. The experimental apparatus have been designed and are being constructed to implement the new experimental designs.

List of Symbols

ρ	fluid density
ϕ	porosity
Φ	potential
μ	viscosity
b	$=\frac{1}{B}$
B	formation volume factor
$\overrightarrow{g}$	earth gravity acceleration
J	objective function
k_r	relative permeability
$k, \mathbf{k}, K$	absolute permeability
N_x	number of blocks in x direction
N_y	number of blocks in y direction
N_z	number of blocks in z direction
N_v	number of positions where velocity data are acquired
N_k	number of grid points where permeability is evaluated
p	pressure
q	sink or source inside the domain
S	saturation in section
t	time
T	transmissibility
$\overrightarrow{v_i}$	filtration velocity
i	spatial index in x direction
j	spatial index in y direction
k	spatial index in z direction
$\mathbf{v}$	velocity
V	volume

Superscript :

n	time step index

obs	experimentally observed value
$calc$	calculated value
$true$	true value

Subscript :

b	bulk
c	capillary
f	index
H	horizonal plane
i	refers to ith component
l	refers to the index of block communicating with a given source and sink
nw	the nonwetting phase
o	oil
t	indicated time
V	vertical plane
w	the wetting phase

References

Alvarado, F. L. (1993). The sparse matrix manipulation system, user and reference manual. URL address: http://www.cs.indiana.edu/ftp/techreports/tr454.html.

Aziz, K. and A. Settari (1979). *Petroleum Reservoir Simulation*. London: Applied Science Publishers.

Bramley, R. and X. Wang (1995). SPLIB: A library of iterative methods for sparse linear systems. URL address: http://www.elk.itu.edu.tr/ dag/lssmc.html.

Chang, C. T., C. Choi, J. T. Hollenshead, and A. T. Watson (1999, November). NMR characterizations of properties of heterogeneous media. Research Report. U. S. Department of Energy,

Report Number DE-AC26-99BC15202, Texas A&M University.

Chang, C. T., J. T. Hollenshead, and A. T. Watson (2000, December). NMR characterizations of properties of heterogeneous media. Research Report. U. S. Department of Energy, Report Number DE-AC26-99BC15202, Texas A&M University.

Hollenshead, J. T., J. Phan, J. Uh, and A. T. Watson (2001, May). NMR characterizations of properties of heterogeneous media. Research Report. U. S. Department of Energy, Report Number DE-AC26-99BC15202, Texas A&M University.

Nolen, J. S. and D. W. Berry (1972). Test of the stability and time-step sensitivity of semi-implicit reservoir simulation techniques. *Soc. Pet. Eng. J. 12*, 263.

Peaceman, D. W. (1977). *Fundamentals of Numerical Reservoir Simulation*. NewYork: Elsevier Scientific Publishing Company.

Phan, J., J. Uh, R. Valestrand, S. Xue, and A. T. Watson (2001, November). NMR characterizations of properties of heterogeneous media. Research Report. U. S. Department of Energy, Report Number DE-AC26-99BC15202, Texas A&M University.

Saad, Y. (1994). SPARSKIT: a basis tool kit for sparse matrix computations, version 2 . URL address: http://www.cs.umn.edu/research/arpa/sparskit/sparskit.html.

Seto, K. (1999). *Miscible Displacement Simulation and Permeability Characterization in Porous Media*. Ph. D. thesis, Texas A&M University.

Seto, K., J. T. Hollenshead, A. T. Watson, C. T. P. Chang, and J. C. Slattery (2001). Determination permeability determinations using NMR velocity imaging. *Transport in Porous Media*, 351–388.

Slattery, J. C. (1981). *Momentum, Energy, and Mass Transfer in Continue*. New York: Krieger.

Watson, A. T., J. T. Hollenshead, and C. T. P. Chang (2001). Developing nuclear magnetic resonance imaging for engineering applications. *Inverse Problems in Engineering 9*, 487–505.

Watson, A. T., J. T. Hollenshead, J. Uh, and C. T. P. Chang (2002). Nmr determination of porous media property distributions. In G. A. Webb (Ed.), *Annual Reports on NMR Spectroscopy*, pp. 113–144. Elsevier Science Ltd.

Watson, A. T., P. C. Richmond, P. D. Kerig, and T. M. Tao (1988). A regression-based method for estimating relative permeabilities from displacement experiments. *SPE Res. Eng. 3*, 953.